3D Shape and Indirect Appearance By Structured Light Transport

Matthew O'Toole John Mather Kiriakos N. Kutulakos
Department of Computer Science
University of Toronto
{motoole,jmather,kyros}@cs.toronto.edu

Abstract

We consider the problem of deliberately manipulating the direct and indirect light flowing through a time-varying, fully-general scene in order to simplify its visual analysis. Our approach rests on a crucial link between stereo geometry and light transport: while direct light always obeys the epipolar geometry of a projector-camera pair, indirect light overwhelmingly does not. We show that it is possible to turn this observation into an imaging method that analyzes light transport in real time in the optical domain, prior to acquisition. This yields three key abilities that we demonstrate in an experimental camera prototype: (1) producing a live indirect-only video stream for any scene, regardless of geometric or photometric complexity; (2) capturing images that make existing structured-light shape recovery algorithms robust to indirect transport; and (3) turning them into one-shot methods for dynamic 3D shape capture.

1. Introduction

A common assumption in computer vision is that light travels along *direct* paths, *i.e.*, it goes from source to camera by bouncing at most once in the scene. While this assumption works well in many cases, light propagation through natural scenes is actually a much more complex phenomenon: light reflects and refracts, it undergoes specular and diffuse inter-reflections, it scatters volumetrically and creates caustics, and may do all of the above in the same scene. Analyzing all these phenomena with a conventional camera is a hard, open problem—and is even harder when the scene is dynamic and light transport changes unpredictably.

Despite the problem's intrinsic difficulty, indirect transport is a major component of real-world appearance [1] and an important cue for scene and material understanding [2]. It is also a major factor preventing broader use of structured-light techniques, which largely assume direct or low-frequency light transport (*e.g.*, 3D laser scanning [3, 4], active triangulation [5, 6] and photometric stereo [7]).

As a step toward analyzing scenes that exhibit complex light transport, in this paper we develop a framework for imaging them in real time. Our focus is on the general case where the scene is unknown; its motion and photometric properties unrestricted; and its illumination comes from one or more controllable sources in general position (*e.g.*, projectors).

Working from first principles, we show that two families of transport paths dominate image formation in a projector-camera system: *epipolar paths*, which satisfy the familiar epipolar constraint and contribute to a scene's direct image, and *non-epipolar paths* which contribute to its indirect. Crucially, while the contributions of these paths are hard to separate in an image, the paths themselves are easy to untangle in the optical domain *before* acquisition takes place. Using this idea as a starting point, we develop a novel technique called *Structured Light Transport (SLT)* that processes epipolar and non-epipolar paths optically for the purpose of live imaging and 3D shape recovery. In particular, we define and address four imaging problems:

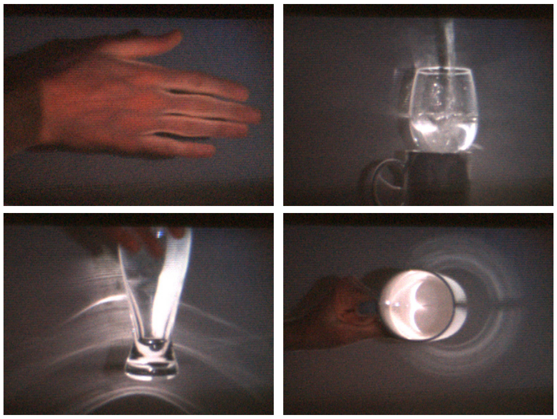

Figure 1: Snapshots from raw live indirect video. Clockwise from top: (1) A hand; note the vein pattern and the inter-reflections between fingers. (2) Pouring water into a glass. (3) Caustics formed inside a mug from specular inter-reflections; note the secondary reflections to the board behind the mug and from the board onto the mug's exterior surface. (4) Refractions and caustics from a beer glass. See Figure 9 for more images and [8] for videos.

- **one-shot indirect-only imaging:** capture an image that records only contributions from indirect light;
- **one-shot indirect-invariant imaging:** given any desired illumination, capture an image where light appears to have been transported by direct paths only;
- **two-shot direct-only imaging:** capture two images whose difference contains only the direct light; and
- **one-shot multi-pattern imaging:** given any $N \geq 2$ desired illuminations, capture an image that "packs" into one shot N separate views of the scene, each corresponding to a desired illumination.

Little is currently known about how to solve these problems in the general setting we consider. Our solutions, while firmly rooted in computer vision, operate exclusively in the optical domain and require no computational post-processing: our implementation is a physical device that just outputs live video; this is optionally processed "downstream" by standard 3D reconstruction algorithms [5] which can be oblivious to the complexity of light transport occurring in a scene. The device itself is a novel combination of existing off-the-shelf components—a conventional video camera operating at 28Hz, a pair of synchronized digital micro-mirror devices (DMDs) operating at 2.7kHz to 24kHz, and optics for coupling them.

From a practical point of view, our work offers four main contributions over the state of the art. First, it is the first demonstration of an "indirect-only video camera," *i.e.*, a camera that outputs a live stream of indirect-only video for fully-general scenes—exhibiting arbitrary motion, caustics, specular inter-reflections and numerous other transport effects. Prior work on indirect imaging was either constrained to static scenes [9, 10], or assumed diffuse/low-frequency transport [2, 11] and accurate 2D motion estimation [11]. Second, we show how to capture—with just one SLT shot—views of a scene that are invariant to indirect light. This is particularly useful for imaging dynamic scenes and represents an advance over direct-only imaging [2, 9], which requires at least two images. Third, we show that *any* ensemble of structured-light patterns can be made robust to indirect light, regardless of the patterns' frequency content. This involves simply switching from conventional to SLT imaging—without changing the patterns or the algorithm that processes them. As such, our work stands in contrast to prior work on transport-robust structured light, which places the onus on the design of the patterns themselves [6, 12–14]. Fourth, we show that SLT imaging can turn any multi-pattern 3D structured-light method into a one-shot technique for dynamic shape capture. Thus an entire family of previously-inapplicable techniques can be brought to bear on this much-studied problem [5, 15–18] in order to improve depth map resolution and robustness to indirect light. As a proof of concept, we demonstrate in Figure 9 the reconstruction of dense depth and albedo from individual frames of monochrome video, acquired by combining indirect-invariant SLT imaging and conventional six-pattern phase-shifting.

Conceptually, our work has one essential difference from conventional structured light [2, 5]: instead of controlling light only at its source by projecting patterns, we control light at its destination as well, with a DMD mask in front of the camera pixels. This simultaneous projection and masking makes it possible to analyze light transport *geometrically* (by blocking 3D light paths), rather than *photometrically* (by blocking certain transport frequencies and assuming constrained scene reflectance [2]). It also enables optical-domain implementations, which can have a significant speed and signal-to-noise ratio advantage over post-capture processing. The idea was first used in [9] for static scenes and a coaxial projector/camera, where epipolar geometry is degenerate and stereo is impossible. While SLT imaging builds on that work, its premise, theory, applications, and physical implementation are different.

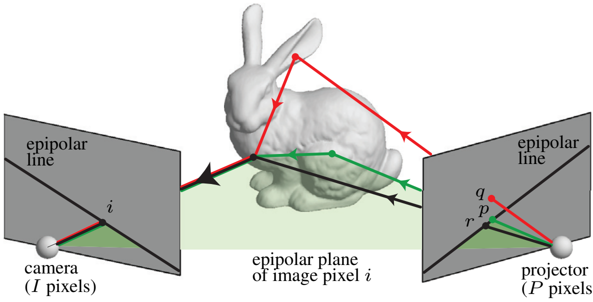

Figure 2: Light transport in a stereo projector-camera system. Light can reach pixel i on the image in one of three general ways: by indirect transport from an arbitrary pixel p on the corresponding epipolar line (green path); by indirect transport from a pixel q that is *not* on that line (red path); or by direct surface reflection, starting from projector pixel r on the epipolar line (black path).

2. The Stereo Transport Matrix

We begin by relating scene geometry to the light transported from a projector to a camera in general position. Consider a scene whose shape potentially varies with time. If the camera and projector respond linearly to light, the scene's instantaneous image satisfies the light transport equation [19]:

$$\mathbf{i} \;=\; \mathbf{T}\,\mathbf{p} \qquad (1)$$

where $\mathbf{i}$ is the image represented as a column vector of I pixels; $\mathbf{p}$ is the P-pixel projected pattern, also represented as a column vector; and $\mathbf{T}$ is the scene's $I \times P$ instantaneous light transport matrix.

Intuitively, element $\mathbf{T}[i,p]$ of the transport matrix specifies the total radiance transported from projector pixel p to image pixel i over all possible paths. As such, $\mathbf{T}$ models image formation in very general settings: the scene may have non-Lambertian reflectance, it may scatter light volumetrically, exhibit specular inter-reflections, *etc.*

Anatomy of the stereo transport matrix Since a projector and a camera in general position define a stereo pair, their transport matrix is best understood by taking two-view geometry into account. More specifically, we classify the elements of $\mathbf{T}$ into three categories based on the geometry of their transport paths (Figure 2):

- **Epipolar elements,** whose projector and camera pixels are on corresponding epipolar lines. These are the only elements of $\mathbf{T}$ whose transport paths begin and end on rays that can intersect in 3D. By performing stereo calibration [20] and vectorizing patterns and images according to Figure 3, these elements can be made to occupy a known, time-invariant, block-diagonal subset of the transport matrix.

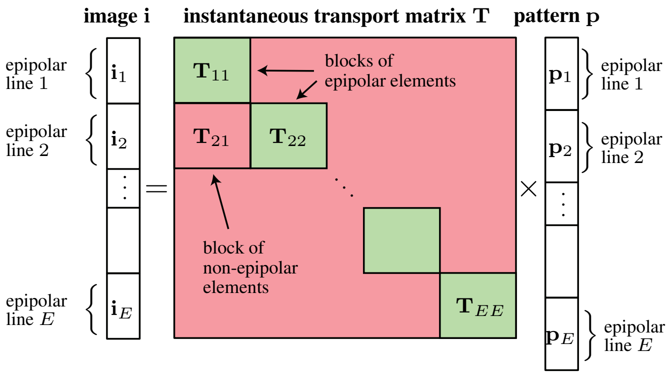

Figure 3: The light transport equation when patterns and images are vectorized so that consecutive pixels on corresponding epipolar lines form subvectors $\mathbf{p}_e$ and $\mathbf{i}_e$, respectively. Under this vectorization scheme, block $\mathbf{T}_{ef}$ of the transport matrix describes transport from epipolar line f on the pattern to epipolar line e on the image. Blocks $\mathbf{T}_{ee}$, shown in green, contain the epipolar elements.

- **Non-epipolar elements**, whose projector pixel and camera pixel are not on corresponding epipolar lines. Non-epipolar elements are significant because they vastly outnumber the other elements of $\mathbf{T}$ and *never* account for direct transport. This is because their transport paths begin and end with rays that do not intersect, so light must bounce at least twice to follow them.
- **Direct elements,** whose camera and projector pixels are in stereo correspondence, *i.e.*, they are the perspective projections of a visible surface point. Direct elements are where direct surface reflection actually occurs in the scene; although they always lie within $\mathbf{T}$'s epipolar blocks, their precise location is scene dependent and thus unknown. Indeed, locating the direct elements is equivalent to computing the scene's instantaneous stereo disparity map (Figure 4).

We can therefore express every image of the scene as a sum of three components that arise from distinct "slices" of the transport matrix:

$$\mathbf{i} = \underbrace{\mathbf{T}^{\mathrm{D}}\,\mathbf{p}}_{\text{direct image}} + \underbrace{\mathbf{T}^{\mathrm{EI}}\,\mathbf{p}}_{\substack{\text{epipolar}\\ \text{indirect image}}} + \underbrace{\mathbf{T}^{\mathrm{NE}}\,\mathbf{p}}_{\substack{\text{non-epipolar}\\ \text{indirect image}}} \tag{2}$$

where the $I \times P$ matrices $\mathbf{T}^{\mathrm{D}}$, $\mathbf{T}^{\mathrm{EI}}$ and $\mathbf{T}^{\mathrm{NE}}$ hold the direct, epipolar indirect, and non-epipolar elements, respectively, and are zero everywhere else.

3. Dominance of Non-Epipolar Transport

Although in theory all three image components in Eq. (2) may contribute to scene appearance, in practice their contributions are not equal. The key observation underlying our work is that the non-epipolar component is very large relative to the epipolar indirect for a broad range of scenes:

$$\mathbf{i} \approx \underbrace{\mathbf{T}^{\mathrm{D}}\,\mathbf{p}}_{\text{direct image}} + \underbrace{\mathbf{T}^{\mathrm{NE}}\,\mathbf{p}}_{\text{non-epipolar indirect image}} . \tag{3}$$

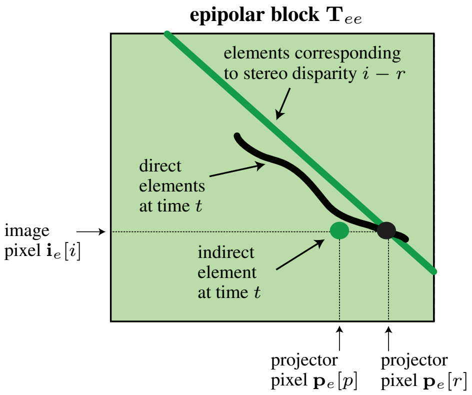
epipolar block $\mathbf{T}_{ee}$
elements corresponding to stereo disparity $i - r$
direct elements at time t
image pixel $\mathbf{i}_e[i]$
indirect element at time t
projector pixel $\mathbf{p}_e[p]$
projector pixel $\mathbf{p}_e[r]$

Figure 4: Structure of an epipolar block $\mathbf{T}_{ee}$. Element $\mathbf{T}_{ee}[i, r]$ describes transport from projector pixel $\mathbf{p}_e[r]$ to image pixel $\mathbf{i}_e[i]$. This element is direct if and only the scene point projecting to both pixels is the same, *i.e.*, the point's stereo disparity is $i - r$. The set of direct elements therefore represents the scene's instantaneous disparity map. Conventional stereo algorithms attempt to localize this set while assuming that the transport matrix is zero everywhere else—both inside and outside its epipolar blocks.

We call this the *non-epipolar dominance assumption*. The transport matrix is much simpler when this assumption holds because we can treat it as having a time-invariant structure with two easily-identifiable parts: the epipolar blocks, which contribute only to the direct image, and the non-epipolar blocks, which contribute only to the indirect.

To motivate this assumption on theoretical grounds, we prove that it holds for two very general scene classes: (1) scenes whose transport function is measurable everywhere and (2) generic scenes containing pure specular reflectors and transmitters. These two cases can be thought of as representing opposite extremes, with the former covering low-frequency transport phenomena such as diffuse interreflection and diffuse isotropic subsurface scattering [21] and the latter covering transport whose frequency content is not band limited. In particular, we prove the following:

Proposition 1. *If* $\mathbf{T}$ *is the discretized form of a transport function that is measurable and positive over the rectified projector and image planes, then*

$$\lim_{\epsilon \to 0} \frac{\mathbf{T}^{\mathrm{EI}}\,\mathbf{p}}{\mathbf{T}^{\mathrm{NE}}\,\mathbf{p}} = \mathbf{0} \tag{4}$$

where division is entrywise and ϵ *is the pixel size for discretization.*

Proposition 2. *Two generic* n*-bounce specular transport paths that originate from corresponding epipolar lines do not intersect for* $n > 1$.

See [8] for proofs. Intuitively, both propositions are consequences of a "dimensionality gap": the set of transport paths contributing to the epipolar indirect image has lower dimension than the set of paths contributing to the non-epipolar image (Figure 2). Thus contributions accumulated in one image are negligible relative to the other in generic settings.

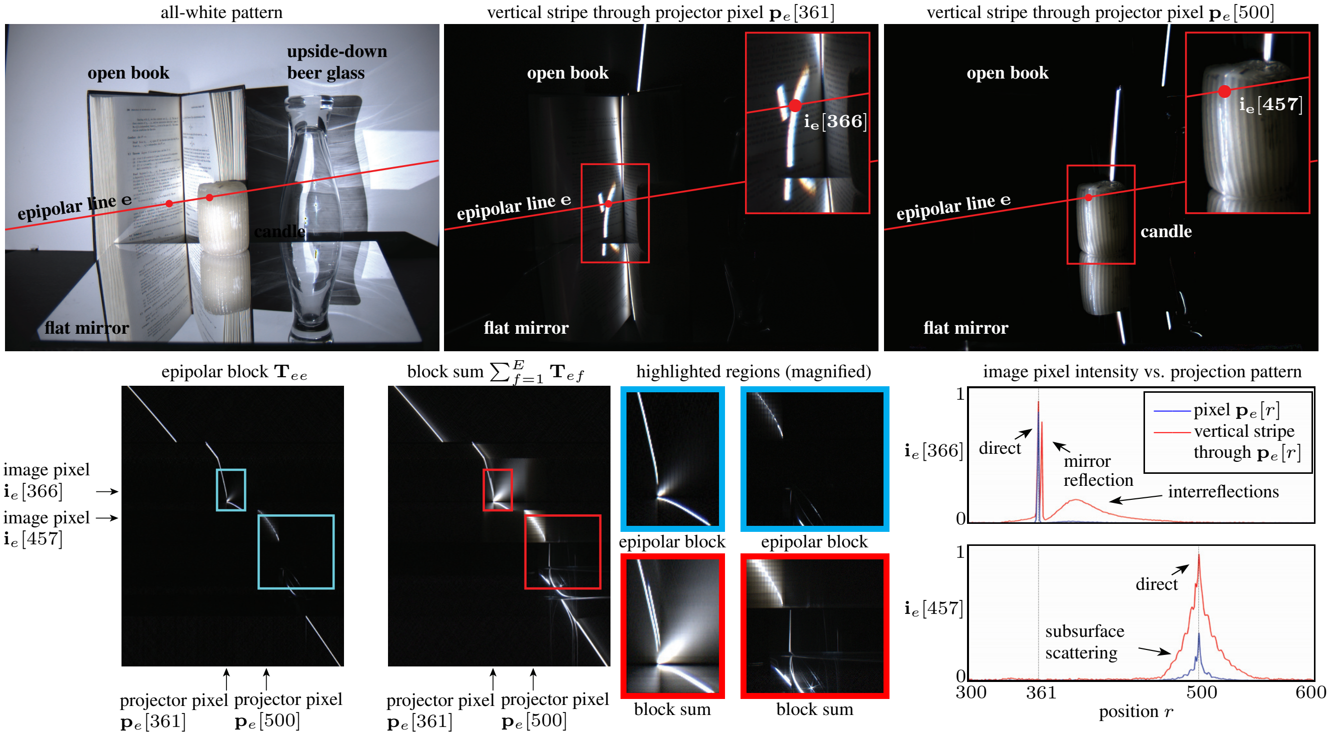

Figure 5: Experimental validation of non-epipolar dominance for a scene containing diffuse, translucent, refractive and mirror-like objects. **Top left:** View under an all-white projection pattern. **Top middle:** View when just one white vertical stripe is projected onto the scene. The many bright regions in this image occur because the stripe illuminates the book's pages in three different ways: (1) directly from the projector, (2) by diffuse inter-reflection from the opposite page, and (3) by specular reflection via the mirror. Their existence makes the scene hard to reconstruct with conventional techniques such as laser-stripe 3D scanning [4]. A magnified view of these regions is shown in the inset. **Top right:** View for another vertical stripe, part of which falls on the candle. The stripe appears very broad and poorly localized there, because of strong sub-surface scattering. **Bottom left:** The epipolar block $\mathbf{T}_{ee}$ for epipolar line e. We show $\mathbf{T}_{ee}$ using the conventions of Figure 4, *i.e.*, its r-th column comes from an image of the scene acquired with only projector pixel $\mathbf{p}_e[r]$ turned on. **Bottom middle:** To assess the image contribution of non-epipolar transport, we acquire the block sum $\sum_{f=1}^{E} \mathbf{T}_{ef}$ and compare it to block $\mathbf{T}_{ee}$—observe that non-epipolar contributions indeed far surpass the epipolar indirect ones. To acquire the block sum, we capture images of the scene while sweeping a vertical stripe on the projector plane (see [8] for a video of the captured image sequence). The r-th column of the block sum is given by the pixels on epipolar line e when the stripe is at $\mathbf{p}_e[r]$. **Bottom right:** Horizontal cross-section of $\mathbf{T}_{ee}$ and $\sum_{f=1}^{E} \mathbf{T}_{ef}$ for two image pixels. Observe that $\mathbf{T}_{ee}$'s cross-section (blue) is sharp and unimodal whereas the block sum's (red) is trimodal for one pixel and very broad for the other.

On the practical side, we have found non-epipolar dominance to be applicable quite broadly; see Figure 5 for a detailed analysis of non-epipolar dominance in a complex scene, Figure 9 for more examples, and [8] for videos confirming the assumption's validity in a variety of settings.

4. Imaging by Structured Light Transport

The rich structure of the stereo transport matrix cannot be exploited by simply projecting a pattern onto the scene. This is because projection gives no control over how light flows through the scene: all elements of $\mathbf{T}$—regardless of position—will participate in image formation. To make full use of $\mathbf{T}$'s structure, *we structure the flow of light itself.*

Our starting point is an imaging procedure first proposed by O'Toole *et al.* [9]. Its main advantage is that the contribution of individual elements of $\mathbf{T}$ can be weighted according to a user-defined "probing matrix" $\mathbf{\Pi}$:

$$\mathbf{i} \;=\; [\,\mathbf{\Pi} \circ \mathbf{T}\,]\,\mathbf{1} \qquad (5)$$

where $\circ$ denotes entrywise (*a.k.a.* Hadamard) product and $\mathbf{1}$ is a column vector of all ones. Images captured this way are said to be the result of *probing* the scene's transport matrix with matrix $\mathbf{\Pi}$. Conceptually, they correspond to images of a scene that is illuminated by an all-white pattern and whose transport matrix is $\mathbf{\Pi} \circ \mathbf{T}$.

Two basic questions arise when considering Eq. (5) for image acquisition and shape recovery: (1) what should $\mathbf{\Pi}$ be, and (2) how to design an imaging system that implements the equation? The answers in [9] were restricted to static scenes and projector/camera arrangements that share a single viewpoint, none of which apply here. Below we focus on the first question—designing $\mathbf{\Pi}$—and discuss live imaging of dynamic scenes in Section 5.

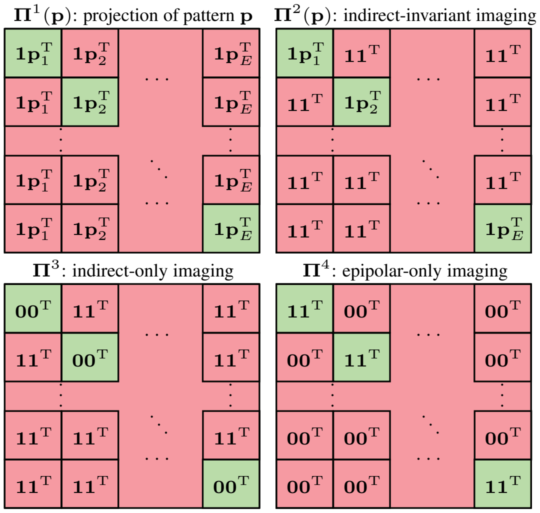
$\mathbf{\Pi}^1(\mathbf{p})$: projection of pattern $\mathbf{p}$
$\mathbf{\Pi}^2(\mathbf{p})$: indirect-invariant imaging
$\mathbf{\Pi}^3$: indirect-only imaging
$\mathbf{\Pi}^4$: epipolar-only imaging
$\mathbf{1p}_1^{\mathrm{T}}$
$\mathbf{1p}_2^{\mathrm{T}}$
$\mathbf{1p}_E^{\mathrm{T}}$
$\mathbf{11}^{\mathrm{T}}$
$\mathbf{00}^{\mathrm{T}}$

Figure 6: The four basic probing matrices used in this paper. Their block structure mirrors the structure of $\mathbf{T}$ in Figure 3.

Conventional structured-light imaging To gain some insight, let us re-cast as a probing operation the act of projecting a fixed pattern $\mathbf{p}$ and capturing an image $\mathbf{i}$. Applying the vectorization scheme of Figure 3 to the light transport equation and re-arranging terms we get for epipolar line e:

$$\mathbf{i}_e = \sum_{f=1}^{E} \mathbf{T}_{ef}\,\mathbf{p}_f = \left[\sum_{f=1}^{E} \underbrace{(\mathbf{1}\mathbf{p}_f^{\mathrm{T}})}_{\substack{\text{block of}\\ \text{probing matrix}}} \circ \underbrace{\mathbf{T}_{ef}}_{\text{block of } \mathbf{T}}\right]\mathbf{1} \qquad (6)$$

where E is the number of epipolar lines. Equation (6) implies that projecting $\mathbf{p}$ is equivalent to probing with the matrix $\mathbf{\Pi}^1(\mathbf{p})$ shown in Figure 6. Observe that if we capture images for a whole sequence of projection patterns—as is often the case in structured-light systems—the non-epipolar blocks of the probing matrix will be different for each pattern. Indirect transport will therefore contribute to each captured image differently, and in a way that strongly depends on the particular pattern. This makes structured-light 3D scanning difficult when indirect transport is present because its contributions cannot be easily identified and removed.

Indirect-invariant imaging The contribution of indirect transport becomes much easier to handle if we ensure it is *the same for every pattern*. Since this contribution is dominated by the non-epipolar blocks of the transport matrix, we can achieve (almost) complete invariance to indirect transport by probing with a matrix whose non-epipolar blocks are independent of $\mathbf{p}$. In particular, probing with the matrix $\mathbf{\Pi}^2(\mathbf{p})$ in Figure 6 yields

$$\mathbf{i}_e = \underbrace{\left[(\mathbf{1}\mathbf{p}_e^{\mathrm{T}}) \circ \mathbf{T}_{ee}\right]\mathbf{1}}_{\text{direct image (depends on } \mathbf{p})} + \underbrace{\left[\sum_{f=1, f\neq e}^{E} \mathbf{T}_{ef}\right]\mathbf{1}}_{\substack{\text{non-epipolar indirect}\\ \text{image (ambient)}}} . \qquad (7)$$

The image in Eq. (7) has two properties: (1) its direct component is identical to the direct component we would get by projecting $\mathbf{p}$ conventionally onto the scene, and (2) its non-epipolar component is independent of $\mathbf{p}$. This independence essentially turns indirect contributions into an "ambient light" term that does not originate from the projection pattern.[1] To see the practical significance of this independence, the second row of Figure 9 compares views of a scene under conventional and one-shot indirect-invariant imaging, for the same projection pattern.

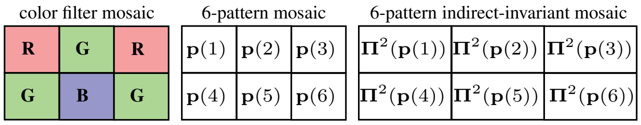
color filter mosaic
R
G
R
G
B
G
6-pattern mosaic
$\mathbf{p}(1)$
$\mathbf{p}(2)$
$\mathbf{p}(3)$
$\mathbf{p}(4)$
$\mathbf{p}(5)$
$\mathbf{p}(6)$
6-pattern indirect-invariant mosaic
$\mathbf{\Pi}^2(\mathbf{p}(1))$
$\mathbf{\Pi}^2(\mathbf{p}(2))$
$\mathbf{\Pi}^2(\mathbf{p}(3))$
$\mathbf{\Pi}^2(\mathbf{p}(4))$
$\mathbf{\Pi}^2(\mathbf{p}(5))$
$\mathbf{\Pi}^2(\mathbf{p}(6))$

Figure 7: Example layouts for color RGB, monochrome 6-pattern, and monochrome 6-pattern indirect-invariant imaging.

An important corollary of Eq. (7) is that indirect-invariant images can be acquired for *any* sequence of patterns—regardless of frequency content or other properties—using the corresponding sequence of probing matrices.

Indirect-only imaging A notable special case of indirect-invariant imaging is to set $\mathbf{p}$ to zero (matrix $\mathbf{\Pi}^3$ in Figure 6). This yields an image guaranteed to have no contributions from direct transport. Moreover, almost all indirect light will be recorded when non-epipolar dominance holds.

Epipolar-only imaging The exact opposite effect can be achieved with a probing matrix that is zero everywhere except along the epipolar blocks (matrix $\mathbf{\Pi}^4$ in Figure 6). When non-epipolar dominance holds, images captured this way can be treated as (almost) purely direct.

One-shot, multi-pattern, indirect-invariant imaging All four probing matrices in Figure 6 produce views of the scene under a fixed illumination pattern $\mathbf{p}$. With probing, however, it is possible to capture—in just one shot—spatially-multiplexed views of the scene for a whole sequence of structured-light patterns, $\mathbf{p}(1), \ldots, \mathbf{p}(S)$. The probing matrix to achieve this can be thought of as defining a "projection pattern mosaic," much like the RGB filter mosaic does for color (Figure 7). Moreover, we can confer invariance to indirect light by defining the mosaic in terms of *probing matrices* rather than conventional patterns.

Specifically, suppose we partition the I image pixels into S sets and let $\mathbf{b}(1), \ldots, \mathbf{b}(S)$ be binary vectors of size I indicating the pixel membership of each set. The matrix

$$\mathbf{\Pi}^5(\mathbf{p}(1), \ldots, \mathbf{p}(S)) = \sum_{s=1}^{S} \left[\, \mathbf{b}(s)\, \mathbf{1}^{\mathrm{T}} \,\right] \circ \mathbf{\Pi}^2(\mathbf{p}(s)) \qquad (8)$$

interleaves the rows of S indirect-invariant probing matrices. Thus, probing with this matrix yields an image containing S sub-images, each of which is a view of the scene under a specific structured-light pattern in the sequence.

[1] Other examples of ambient terms with identical behavior include image contributions from the projector's black level and contributions from light sources other than the projector. Because such terms are often unavoidable yet easy to handle, many structured-light algorithms are designed to either recover them explicitly or be robust to their existence [5]. Non-zero ambient terms do, however, reduce contrast and may affect SNR.

5. Live Structured-Light-Transport Imaging

The feasibility of probing comes from re-writing Eq. (5) as a bilinear matrix-vector product [9]:

$$\mathbf{i} \;=\; \sum_{t=1}^{T} \mathbf{m}(t) \circ [\, \mathbf{T}\, \mathbf{q}(t)\,] \qquad (9)$$

where the transport matrix $\mathbf{T}$ is constant in time and $\mathbf{\Pi} = \sum_{t=1}^{T} \mathbf{m}(t)(\mathbf{q}(t))^{\mathrm{T}}$ is a rank-1 decomposition of the probing matrix. According to Eq. (9), optical probing is possible by (1) opening the camera's shutter, (2) projecting pattern $\mathbf{q}(t)$ onto the scene, (3) using a semi-transparent pixel mask $\mathbf{m}(t)$ to modulate the light arriving at individual camera pixels, (4) changing the pattern and mask synchronously T times, and (5) closing the shutter. This procedure acquires one image; it was implemented in [9] for low-resolution probing matrices using an LCD panel for pixel masking, an SLR camera for image acquisition, and $T \in [100, 1000]$.

Although results were promising, LCDs are not suitable for video-rate (30Hz) probing: they refresh at 30-200Hz, limiting T to an unusable 1-6 masks/projections per frame; and they have low transmittance, requiring long exposure times.

Our approach, on the other hand, is to use a pair of off-the-shelf digital micro-mirror (DMD) devices for projection and masking (Figure 8). These devices are compact, incur no light loss and can operate synchronously at $2.7 - 24$kHz. To implement Eq. (9), we couple them with a conventional video camera operating at 28fps. This allows $96 - 800$ masks/projections within the 36msec exposure of each frame.[2] To our knowledge, such a coupling has not been proposed before.[3]

A major difference between LCDs and DMDs is that DMDs are *binary*. This turns the derivation of masks and projection patterns into a combinatorial optimization problem. Formally, given an *integer*[4] probing matrix $\mathbf{\Pi}$ and an upper bound on T, we seek a length-T rank-1 decomposition into binary vectors such that the decomposition approximates $\mathbf{\Pi}$ as closely as possible. This problem is difficult and we know of no general solution. Indeed, estimating the length of the shortest *exact* decomposition is itself NP-hard [23].

Our approach, below, is to derive randomized decompositions of $\mathbf{\Pi}$ that approximate Eq. (9) in expectation. Although our experience is that this approach works well in practice, it should not be treated as optimal.

Indirect-only imaging Matrix $\mathbf{\Pi}^3$ is a special case where short decompositions are easy. Let $\mathbf{q}(e)$ be a pattern whose pixels are 1 along epipolar line e and 0 everywhere else and let $\mathbf{m}(e)$ be a mask that is 1 everywhere except at epipolar line e. Then it is easy to show that $\mathbf{\Pi}^3 = \sum_{e=1}^{E} \mathbf{m}(e)(\mathbf{q}(e))^{\mathrm{T}}$. This corresponds to a sequence of mask/projection pairs where only one epipolar line is "off" in the mask and only the corresponding epipolar line is "on" in the pattern. Even though this decomposition is exact—and feasible for near-megapixel images—it has poor light efficiency because only one epipolar line is "on" at any time. To improve light efficiency we use random patterns instead, which yield good approximations that are much shorter.

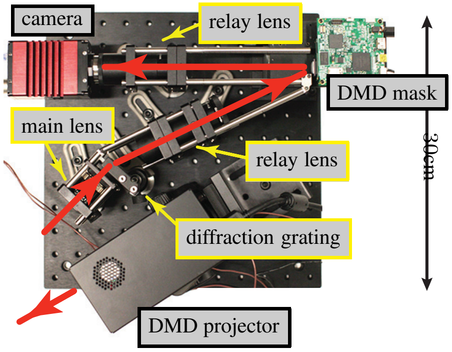

Figure 8: Photo of our prototype. The projector can be detached to change the stereo baseline. The optical path is shown in red. See [8] for a detailed list of components.

Specifically, consider the random pattern

$$\mathfrak{q} = \{\text{each epipolar line is 1 with probability } 0.5\} \;\; , \qquad (10)$$

let the projection pattern $\mathbf{q}(t)$ be a sample of $\mathfrak{q}$, and let the mask $\mathbf{m}(t)$ be equal to $\overline{\mathbf{q}(t)}$. Taking expectations in Eq. (9), the epipolar line e of the expected image is given by

$$\mathcal{E}[\mathbf{i}_e] \;=\; \mathcal{E}[\overline{\mathfrak{q}_e}] \circ \sum_{\substack{f=1 \\ f\neq e}}^{E} \mathbf{T}_{ef}\, \mathcal{E}[\mathfrak{q}_f] \;=\; 0.25 \sum_{\substack{f=1 \\ f\neq e}}^{E} \mathbf{T}_{ef}\, \mathbf{1} \qquad (11)$$

where $\mathcal{E}[]$ denotes expectation. This is the result of probing with matrix $\mathbf{\Pi}^3$, albeit at one quarter of the "ideal" image intensity.[5] Note that corresponding epipolar lines are never on at the same time in the pattern and mask; thus no epipolar transport path ever contributes to the captured image.

Epipolar-only imaging Matrix $\mathbf{\Pi}^4$ is a special case at the other extreme, where *no* short rank-1 decompositions exist. Since $\mathbf{\Pi}^4 = \mathbf{\Pi}^1(\mathbf{1}) - \mathbf{\Pi}^3$, we compute the result of probing with $\mathbf{\Pi}^4$ by subtracting two adjacent video frames—one captured by projecting an all-white pattern and one captured by indirect-only imaging. Naturally, two-frame motion estimation may be necessary to handle fast-moving scenes (but we do not estimate motion in our experiments).

Indirect-invariant imaging A perhaps counterintuitive result is that even though epipolar-only imaging requires two frames, indirect-invariant imaging requires just one. This is important because probing with matrix $\mathbf{\Pi}^2()$ is all we need

[2] See [9] for an analysis of the SNR advantage confered by performing T mask/projection operations in a single exposure versus capturing an image for each projection pattern, at $1/T$-th the exposure.

[3] The closest design we are aware of comes from confocal microscopy [22]. Its optical path was less challenging to implement, however, because imaging was both coaxial and orthographic.

[4] Since any grayscale structured-light pattern $\mathbf{p}$ must be quantized before projection, probing matrices are always integer, including $\mathbf{\Pi}^2(\mathbf{p})$.

[5] Intuitively, since half the epipolar lines are "off" in the pattern and the mask, only 1/4th of the total light is transported from projector to camera.

for reconstruction with structured light. Let $\mathbf{p}$ be an arbitrary structured-light pattern scaled to $[0, 1]$. Define mask $\mathbf{m}(t)$ to be a sample of $\mathfrak{q}$ from Eq. (10) and the pattern to be

$$\mathbf{q}(t) \;=\; \mathbf{m}(t) \circ \mathbf{r}(t) \;+\; \overline{\mathbf{m}(t)} \circ \overline{\mathbf{r}(t)} \tag{12}$$

where $\mathbf{r}(t)$ is a sample of yet another random pattern:

$$\begin{aligned} \mathfrak{r} = \{&\text{pixel } p \text{ on epipolar line } e \text{ is } 1 \\ &\text{with probability } \mathbf{p}_e[p]\} \;\; . \end{aligned} \tag{13}$$

A pictorial illustration of Eq. (12) can be found in [8]. From calculations similar to Eq. (11), the expected image is

$$\begin{aligned} \mathcal{E}[\mathbf{i}_e] \;&=\; 0.5\mathbf{T}_{ee}\mathbf{p}_e + 0.25 \sum_{f=1, f\neq e}^{E} [\mathbf{T}_{ef}\mathbf{p}_f + \mathbf{T}_{ef}(\mathbf{1} - \mathbf{p}_f)] \\ &=\; \underbrace{0.5\mathbf{T}_{ee}\mathbf{p}_e}_{\substack{\text{direct image} \\ \text{(depends on } \mathbf{p})}} \;+\; \underbrace{0.25 \sum_{f=1, f\neq e}^{E} \mathbf{T}_{ef}\mathbf{1}}_{\text{indirect image (ambient)}} \;, \end{aligned} \tag{14}$$

which is equivalent to the result of probing with $\mathbf{\Pi}^2()$.

One-shot, multi-pattern, indirect-invariant imaging Here we use the mask for indirect-invariant imaging and temporally multiplex S random projection patterns—each defined by Eq. (12) and corresponding to a different structured-light pattern— across our "budget" of T total projections per video frame. After the video is recorded, we "demosaic" each frame $\mathbf{i}$ independently to infer S full-resolution images, one for each structured-light pattern. Following work on compressed sensing [24, 25] we do this by solving for S images that reproduce frame $\mathbf{i}$ and are sparse under a chosen basis $\mathbf{W}$:

$$\text{minimize} \;\; \left\| \mathbf{W}^{\mathbf{T}} \left[\mathbf{i}(1) \quad \ldots \quad \mathbf{i}(S) \right] \right\|_n \tag{15}$$

$$\text{subject to} \;\; \left\| \sum_{s=1}^{S} \mathbf{b}(s) \circ \mathbf{i}(s) - \mathbf{i} \right\|_2 \leq \epsilon \tag{16}$$

where $\|.\|_n$ is a sparsity-inducing norm[6] and $\mathbf{b}(s)$ is the binary vector holding pixel memberships for pattern s.

6. Experimental Results

Indirect-only and epipolar-only imaging Our DMDs operated at 2.7kHz with $T = 96$ or 48 patterns/masks per frame. For calibration, we computed the epipolar geometry between the two DMDs by first relating them to the image plane. Overall resolution was equal to the resolution of our DMDs, *i.e.*, 608×684. See Figures 1 and 9 (row 1) for examples of indirect- and epipolar-only images, respectively.

Indirect-invariant imaging We used high-end DMDs and a monochrome camera for the reconstruction experiments in Figure 9 (rows 2 and 3), with $T = 800$ patterns/masks per frame. The effective DMD resolution was approximately 484×364. The scenes occupied a $40^3 cm^3$ volume about $70cm$ away from the camera. To show the effectiveness of SLT imaging, we chose the most basic pattern and technique—phase-shifting with 9 sinusoids total, at frequencies 1, 8 and 64.

Dense depth and albedo from one shot We used $S = 6$ sinusoids at frequencies 4 and 32 for the experiment in Figure 9 (row 4), and a random, rather than regular, assignment of pixels to sinusoids. We recorded multi-pattern, indirect-invariant video at 28fps and reconstructed each frame independently by (1) solving for the 6 demosaiced patterns using SPGL1 [26] for optimization and the JPEG2000 wavelet basis, and (2) using them to get per-pixel depth and albedo.

7. Concluding Remarks

We believe that optical-domain processing—and SLT imaging in particular—offers a powerful new way to analyze the appearance of complex scenes, and to boost the abilities of existing reconstruction algorithms. Although our focus was mainly on monochromatic light and conventional cameras, SLT imaging depends on neither; integrating this framework with other imaging dimensions (polarization, wavelength, time, *etc.*) is a promising direction. Last but not least, although our prototypes rely on DMD masks and several optical components, these would be rendered unnecessary if per-pixel processing was implemented directly on the sensor [27, 28]. We are looking forward to the wide availability of such technologies.

Acknowledgements We are grateful for the support of the Natural Sciences and Engineering Research Council of Canada under the PGS-D, RGPIN, RTI, SGP and GRAND NCE programs.

References

[1] P. Debevec, *et al.* Acquiring the reflectance field of a human face. *Proc. SIGGRAPH'00*.

[2] S. K. Nayar, *et al.* Fast separation of direct and global components of a scene using high frequency illumination. *Proc. SIGGRAPH'06*.

[3] G. Godin, M. Rioux, J. Beraldin, and M. Levoy. An assessment of laser range measurement on marble surfaces. *Proc. 5th Conf. on Optical 3D Measurement Techniques*, 2001.

[4] B. Curless and M. Levoy. Better optical triangulation through spacetime analysis. *Proc. ICCV'95*.

[5] J. Salvi, S. Fernandez, T. Pribanic, and X. Llado. A state of the art in structured light patterns for surface profilometry. *Pattern Recogn*, 43(8):2666–2680, 2010.

[6] M. Gupta, S. Nayar. Micro Phase Shifting. *Proc. CVPR'12*.

[7] S. K. Nayar, K. Ikeuchi, and T. Kanade. Shape from Interreflections. *Int. J. Computer Vision*, 6(3):173–195, 1991.

[8] M. O'Toole, J. Mather, and K. N. Kutulakos. Supplementary materials. *http://www.dgp.toronto.edu/~motoole/slt*.

[9] M. O'Toole, R. Raskar, K. N. Kutulakos. Primal-dual coding to probe light transport. *Proc. SIGGRAPH'12*.

[10] A. Velten, *et al.* Femto-photography: capturing and visualizing the propagation of light. *Proc. SIGGRAPH'13*.

[11] S. Achar, S. T. Nuske, S. G. Narasimhan. Compensating for Motion During Direct-Global Separation. *Proc. ICCV'13*.

[12] M. Gupta, *et al.* Structured light 3D scanning in the presence of global illumination. *Proc. CVPR'11*.

[13] V. Couture, N. Martin, and S. Roy. Unstructured light scanning to overcome interreflections. *Proc. ICCV'11*.

[6] We use the $(1, 2)$-norm because it promotes group sparsity and thus concentrates non-zero terms to the same pixels across views.

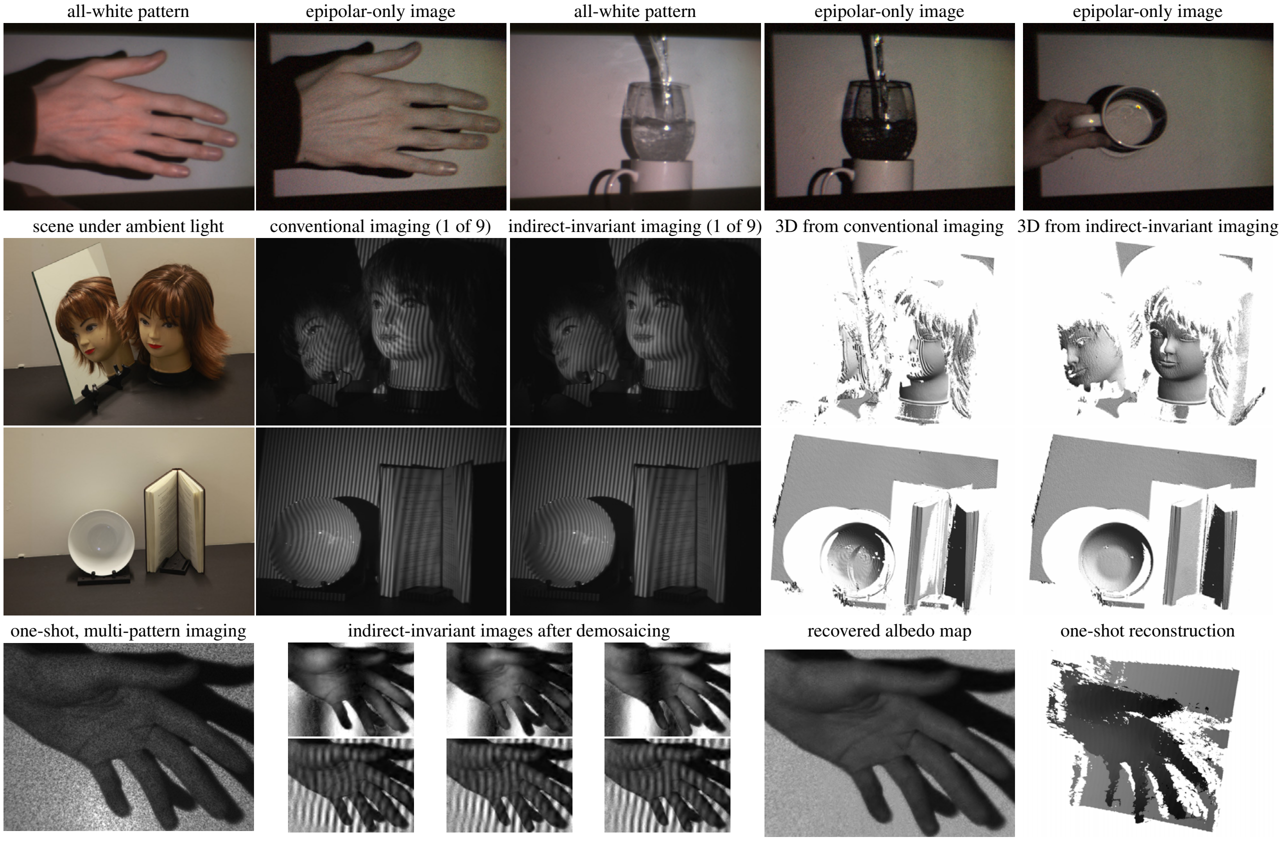

all-white pattern

epipolar-only image

all-white pattern

epipolar-only image

epipolar-only image

scene under ambient light

conventional imaging (1 of 9)

indirect-invariant imaging (1 of 9)

3D from conventional imaging

3D from indirect-invariant imaging

one-shot, multi-pattern imaging

indirect-invariant images after demosaicing

recovered albedo map

one-shot reconstruction

Figure 9: Row 1: Frames from conventional and epipolar-only video for the scenes in Figure 1. Compared to Figure 1, the water's opaque appearance in the epipolar-only frame and the absence of caustics in the mug confirm that significant indirect light was not recorded, *i.e*., non-epipolar dominance holds. Refer to [8] for videos of several more scenes. **Row 2:** We imaged the scene on the left in two ways: (1) projecting 9 phase-shifted patterns directly onto it and (2) capturing indirect-invariant images for the same patterns. Exposure time was held fixed, giving an SNR advantage to conventional projection which does not mask pixels. We then applied the same algorithm to the two sets of images, with the results shown on the right. The algorithm fails catastrophically for the conventionally-acquired images whereas with SLT imaging it is able to reconstruct even the hidden side of the face, from the mirror's indirect view. Closer inspection of the input images (please zoom in) reveals the reason for the difference: the conventional image contains "double fringes" from secondary reflections whereas the indirect-invariant one does not. **Row 3:** Another example, for a scene with strong diffuse and specular inter-reflections. **Row 4:** Reconstructing dense depth and albedo from one video frame of a moving hand. From this frame, our demosaicing algorithm recovers 6 full-resolution indirect-invariant images of the hand, for 6 sinusoidal patterns. These images yield the albedo and depth maps on the right.

[14] T. Chen, H.-P. Seidel, and H. P. A. Lensch. Modulated phase-shifting for 3D scanning. *Proc. CVPR'08*.

[15] L. Zhang, B. Curless, and S. M. Seitz. Rapid shape acquisition using color structured light and multi-pass dynamic programming. In *Proc. 3DPVT*, pages 24–36, 2002.

[16] H. Kawasaki, R. Furukawa, R. Sagawa, and Y. Yagi. Dynamic scene shape reconstruction using a single structured light pattern. *Proc. CVPR'08*.

[17] C. Hernandez, *et al*. Non-rigid Photometric Stereo with Colored Lights. *Proc. ICCV'07*.

[18] G. Fyffe, X. Yu, and P. Debevec. Single-shot photometric stereo by spectral multiplexing. *Proc. ICCP'11*.

[19] R. Ng, R. Ramamoorthi, and P. Hanrahan. All-frequency shadows using non-linear wavelet lighting approximation. *Proc. SIGGRAPH'03*.

[20] R. Hartley and A. Zisserman. *Multiple View Geometry in Computer Vision*. Cambridge University Press, Dec. 2000.

[21] H. Jensen, *et al*. A practical model for subsurface light transport. *Proc. SIGGRAPH'01*.

[22] R. Heintzmann, *et al*. A dual path programmable array microscope (PAM). *J. Microscopy*, 204:119–135, 2001.

[23] J. Zhong. Binary ranks and binary factorizations of nonnegative integer matrices. *Electron. J. Linear Algebra*, 23:540–552, 2012.

[24] D. Reddy, A. Veeraraghavan, and R. Chellappa. P2C2: Programmable pixel compressive camera for high speed imaging. *Proc. CVPR'11*.

[25] Y. Hitomi, J. Gu, M. Gupta, T. Mitsunaga, and S. K. Nayar. Video from a single coded exposure photograph using a learned over-complete dictionary. *Proc. ICCV'11*.

[26] E. van den Berg and M. P. Friedlander. SPGL1: A solver for large-scale sparse reconstruction. *http://www.cs.ubc.ca/~mpf/spgl1*.

[27] M. W. Kelly and M. H. Blackwell. Digital-pixel FPAs enhance infrared imaging capabilities. *Laser Focus World*, 49(1):90, 2013.

[28] G. Wan, *et al*. CMOS Image Sensors With Multi-Bucket Pixels for Computational Photography. *IEEE J. Solid State Circuits*, 47(4):1031–1042, 2012.